Acta Cryst. (1989). A45, 264–268

A HREM Study of the Intergrowth of Magnetite and Coulsonite

BY Y. G. WANG, H. Q. YE, L. L. XIMEN* AND K. H. KUO†

Laboratory of Atomic Imaging of Solids, Institute of Metal Research, Academia Sinica, 110015 Shenyang, People's Republic of China

(*Received* 19 *April* 1988; *accepted* 13 *October* 1988)

Abstract

The microstructures of magnetite containing vanadium and titanium, found in Sichuam province, China, have been studied by high-resolution electron microscopy (HREM). The [1$\bar{1}$0] structural images showed a multiply intimate intergrowth of magnetite and coulsonite as a result of exsolution along the [110] direction instead of the [111] direction as reported previously. The detectable different contrast of the two phases was confirmed by image simulation. The antiphase domain and various stacking faults related to the nonstoichiometry of the transition-metal oxide in the same direction were also observed in magnetite and coulsonite, respectively. The possible genetic aspect and formation of these defects on exsolution are also considered.

1. Introduction

Natural magnetite is usually found to be in coexistence with spinel minerals, oxides and silicates, thus their parallel intergrowth can easily occur; the most probable interfaces between magnetite and spinel minerals are {111} planes. Baker & Whelan (1968) found domain structures and dislocation networks in an intermediate phase as well as the partially transformed crystal during the transformation from hematite to magnetite by transmission electron microscopy (TEM). Dieckmann & Schmalzried (1977) and Dieckmann (1982) studied the defects and cation diffusion in magnetite by thermogravimetry and found that the iron cations could present as interstitials and vacancies, so nonstoichiometry and point defects may come into existence in magnetite. Coulsonite has the same structure as magnetite but a different unit-cell constant owing to the presence of vanadium (about 9%) and/or titanium (about 7%). Coulsonite is often found in magnetite in a random way and the interface between them is the (111) plane (Runble, 1976). High-resolution electron microscopy (HREM) can give insight of this kind of intergrowth at a unit-cell or subunit-cell level. The arrangement of iron cations in magnetite can be revealed and some defect structures related to the arrangements of these iron cations have also been studied.

2. Experimental

The black and magnetic particles of the magnetite found in Sichuan province, China, were first crushed into fragments in an agate mortar and then were made a suspension in absolute alcohol by a supersonic vibrator. This suspension was put on holey carbon films on a microgrid. The observation was accomplished with a JEM-200CX electron microscope equipped with a top-entry goniometer stage having an interpretable point resolution of 2·6 Å. Various crystals with the [1$\bar{1}$0] orientation were chosen so that the image always includes the [111] direction, which makes it easy to identify the intergrowth of magnetite and coulsonite or possibly other spinel minerals. All high-resolution images were taken under the symmetrical incidence condition.

3. Structure of magnetite and image simulation

Magnetite has the inverse-spinel structure, space group $Fd\bar{3}m$, with $a = 8{\cdot}396$ Å for Fe_3O_4 synthesized in the laboratory (Hägg, 1953). However, the unit-cell parameter of the natural mineral may deviate somewhat from this value owing to the presence of some impurities in them. Fig. 1(*a*) shows a schematic view of magnetite along the [1$\bar{1}$0] direction. The arrangement of iron cations forms the distorted hexagons connected side by side and the oxygen atoms form the basic framework of the structure of magnetite or spinel. The structure of coulsonite can be derived from Fig. 1(*a*) by replacing the iron cations with vanadium cations (Radtke, 1962).

In order to interpret the observed image unambiguously, the simulated images of magnetite were calculated based upon the multislice program written by Ishizuka (1982). The parameters used for the image simulation are: the half-width of a Gaussian spread of focus at the experimental gun bias, 70 $Å^{-1}$; the semi-angle of convergence of the incident beam, $\theta_c/\lambda = 0{\cdot}03$ rad $Å^{-1}$; and the size limited by the objective aperture, $(\sin\theta)/\lambda = 0{\cdot}350$ $Å^{-1}$. From the simulated images it is known that at a thickness from 50

* Also at Beijing Graduate School of Geology, Beijing, People's Republic of China.

† Also at Beijing Laboratory of Electron Miscroscopy, Academia Sinica, PO Box 2724, 100080 Beijing, People's Republic of China.

0108-7673/89/040264-05$03.00

to 150 Å and a defocus value from −550 to −750 Å, the bright contrast areas in the [1$\bar{1}$0] image (Fig. 1*b*) correspond to the positions of the iron atoms in the centres of hexagons. The observed image and simulated image (inset) are shown in Fig. 2 where the bright dots in the observed and simulated images match well and there is a direct interpretation of the observed image taken at the Scherzer defocus (Δf = −670 Å). The one-to-one correspondence suggests that the imaging of atoms in this case represents the direct projection of the structure.

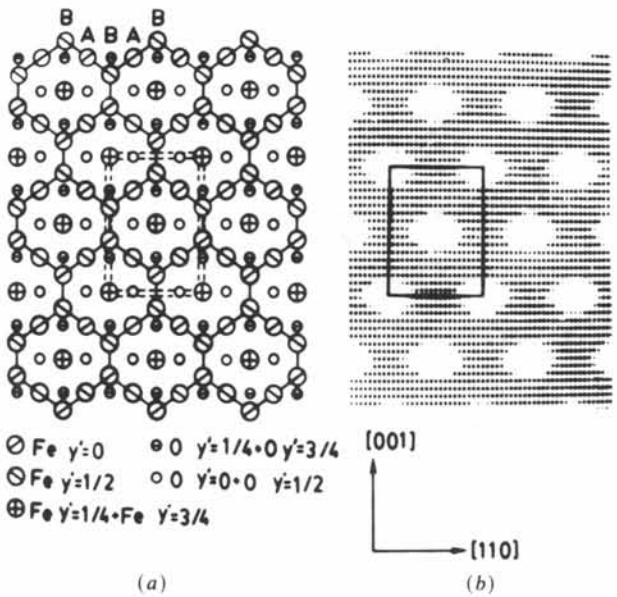

Fig. 1. (*a*) Projection of magnetite along the [1$\bar{1}$0] direction showing the arrangement of the iron atoms forming distorted hexagons, where the iron atoms at the centres and edges of the hexagons are in octahedrally coordinated positions, and the others at the corners of the hexagons are in tetrahedrally coordinated positions. A unit cell is outlined by double dashed lines. (*b*) The simulated image in the same direction calculated at the Scherzer defocus Δf = −650 Å and a thickness of 100 Å shows the correspondence between the bright dots in the image and the iron atoms located at the centres of hexagons in the projected model.

4. Results and discussion

4.1. *Intergrowth as a result of exsolution and antiphase domain*

The intergrowth of two phases having parallel interfaces may cause one-dimensional disorder so that streaks perpendicular to this interface will appear in the electron diffraction pattern (Fig. 3). In this pattern the 002 spot appears as a result of multiple diffractions. Qualitative analysis of the same field by energy-dispersive X-ray analysis shows that in addition to iron and vanadium some titanium and manganese are also present. The corresponding HREM image (Fig. 4) shows a general view of the parallel

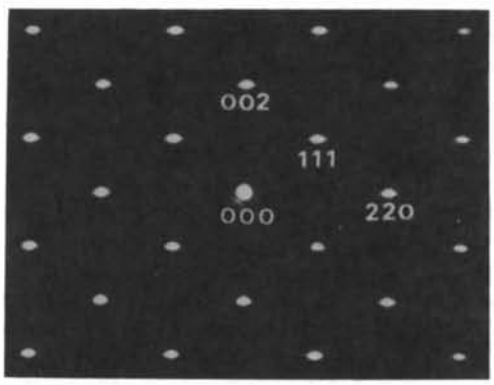

Fig. 3. [1$\bar{1}$0] electron diffraction pattern of magnetite in which the 002 spot appears due to multiple diffractions, and streaks in the [110] direction occur owing to the intergrowth of magnetite and coulsonite.

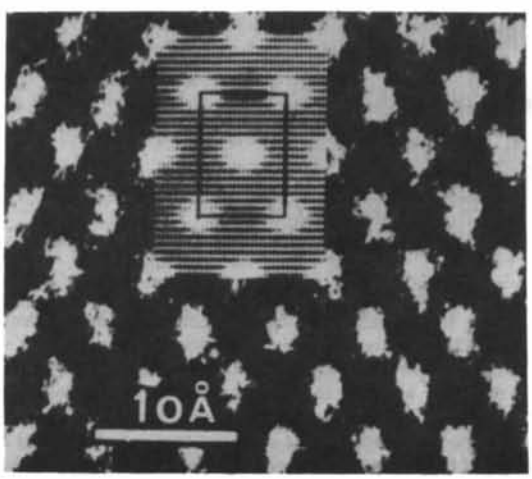

Fig. 2. A [110] HREM image of magnetite taken at the Scherzer defocus with an inserted simulated image which matches well the observed one.

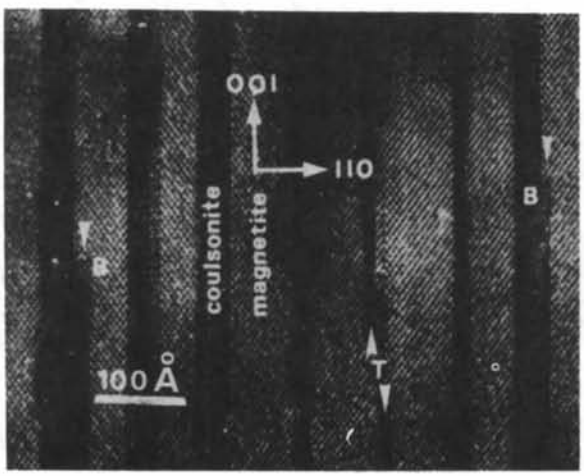

Fig. 4. A general view of the intergrowth of magnetite and coulsonite with (110) interfaces. *B* shows the intergrowth ledges on (001) and *T* the terminated laths of coulsonite.

intergrowth of magnetite and coulsonite with different contrast along the [110] direction and this multiple intergrowth with (110) as the interface forms a compositional modulation wave. The *B* areas labelled by arrows are the intergrowth ledges and *T* areas the terminated laths. It is known that the two phases have the same arrangement of atoms and nearly the same unit-cell parameter so that a coherent interface can be predicted. An enlarged HREM image (Fig. 5) shows the (110) coherent interface (*P*) where the dots with different contrast are arranged in the same manner at both sides and are continuous through the interfaces, whereas at the interface marked *A* the dots are arranged irregularly compared with the *P* areas, *i.e.* a planar fault has been introduced. The model of a planar fault (Fig. 6) can be derived from Fig. 1(*a*) by a slip of the atoms on layer *B* by $c/2$ along the [001] direction in the (110) plane. It can be seen that there is 180° phase difference between the two domain variants and this is coincident with the [110] antiphase domain structure in magnetite. Therefore, the [110] parallel domain structure is caused by such movement of atoms. It is important to note that the basic framework constructed by the oxygen atoms after such a slip remains the same because $c/2$ is a periodic distance for this framework and the coordination of all moved iron atoms is also unchanged. Therefore, the configuration of the (110) boundary of the antiphase domain is a conservative one.

Fig. 7 is the simulated image based on Fig. 6. In this case one and half unit cells at both sides of the domain boundary are taken into consideration so that a total of 112 atoms are contained and the periodic extension of 20·8 Å is actually along the [110] direction. Contrast in the two domain variants is the same and different contrast can be seen in Fig. 7(*b*) when the right domain variant including the domain boundary (layer *A* in Fig. 6) is replaced by coulsonite which exhibits a darker contrast than magnetite. This difference in contrast is detectable for wider ranges of crystal thickness and defocus value. Sometimes

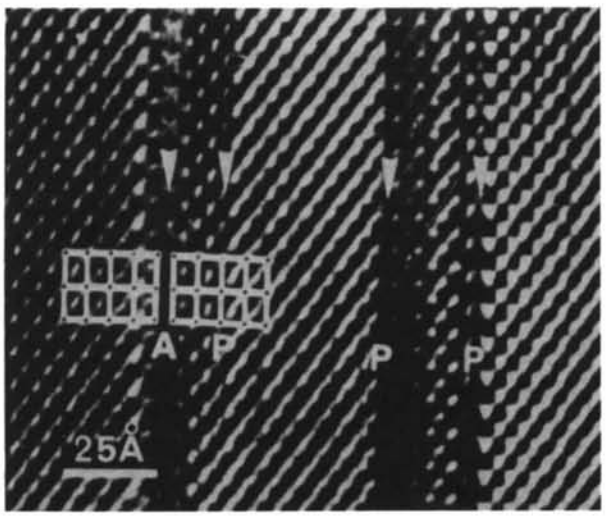

Fig. 5. [1$\bar{1}$0] structural image showing (110) coherent interfaces (*P*) of magnetite and coulsonite. A planar fault can be observed at the interface marked *A*.

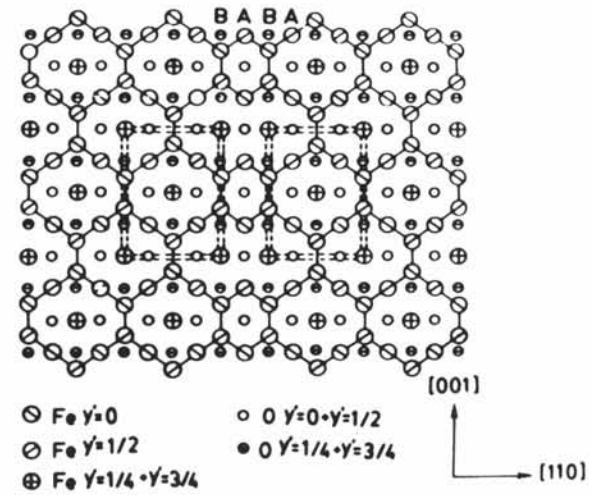

Fig. 6. Schematic diagram of the [110] antiphase domain of magnetite (see *A* in Fig. 5).

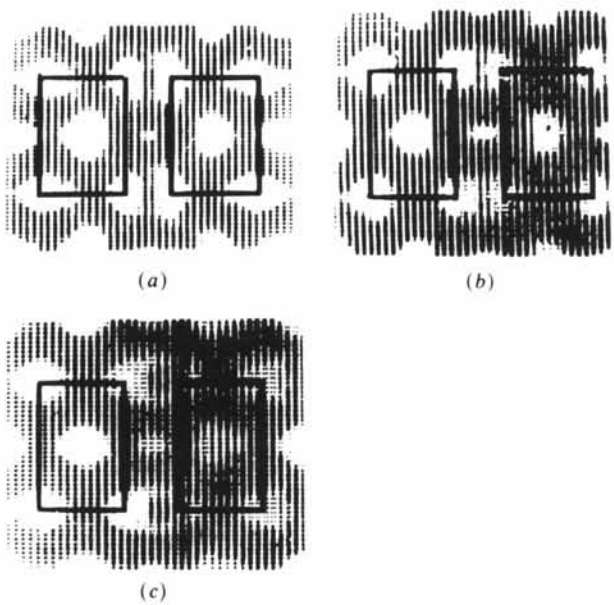

Fig. 7. (*a*) Image calculated from the structure model shown in Fig. 6. When the right domain is replaced by coulsonite, it shows a dark contrast (*b*) and (*c*). The conditions used in (*a*) and (*b*) are the same as those in Fig. 1(*b*), while (*c*) was calculated at $\Delta f = -780$ Å and $t = 50$ Å showing only a small change of contrast in background, but the different contrast of the dots in the image of the two parts is nearly the same. This suggests that the co-existence of two phase can be directly detected by the arrangement of dots with different contrast in the HREM image. These figures are all a periodic distance along the [110] direction used in the calculation.

there is only a small change of contrast in the background and the brightness of the dots of the two different domains is nearly the same (Fig. 7*c*). Through the different scattering power of vanadium and iron atoms to electrons, the contrast becomes darker for the presence of vanadium with stronger scattering power in the area of coulsonite and it seems to be enhanced with increase of the sample thickness in the calculation.

The two mechanisms of exsolution have been shown by Gibbs (1948) and Cahn (1968) and here a possible genetic explanation of the observed microstructure may be that the coulsonite exsoluted by nucleation on cooling. Since magnetite and coulsonite share a common framework of oxygen atoms, a coherent relationship is predicted to be maintained between the matrix and precipitate and the nucleation of coulsonite could occur uniformly throughout the crystal, as in the case of homogeneous nucleation. The energy of formation of a new phase could be reduced by nucleation on a pre-existing defect, such as a grain boundary or dislocation where heterogeneous nucleation could easily take place. The antiphase boundary and other planar faults (to be discussed below) may be favourable sites for the formation of coulsonite. These grew into parallel laths along the [100] direction which is also the direction of these defects. Therefore, (110) instead of (111), which is usually the case in the f.c.c crystals, becomes the interface. The termination of laths and the wave-like microstructure imply that they are the result of multiple nucleation and indicate that the decomposition is well advanced, although the microstructure is still very fine.

4.2. *Stacking faults related to nonstoichiometry*

If the formation of the interface involves only the replacement of the different cations or the rearrangement of the same kind of cations, the boundaries formed during the crystal growth or phase transform are conservative and the chemical composition at the boundaries remains unchanged. Otherwise the boundaries are nonconservative. Fig. 8 shows these boundaries indicated by *P*, *E* and *D*, respectively. *D* indicates the nonconservative interfaces between magnetite and coulsonite where there is 1/4[111] displacement of the dots. Fig. 9 shows a possible arrangement of cations at the boundary *D*, where there are two layers of *A*-type stacking sequentially along the [110] direction. So it is indeed a stacking fault. But it should be pointed out that this stacking fault cannot be produced by shear stresses because the *A* and *B* layers are not equivalent to each other and the ratio of the iron and oxygen atoms at the fault plane is different from that in the matrix and this ratio cannot be varied by slip. In the matrix the ratio of iron and oxygen atoms is 3:4, whereas it becomes 2:3 at the fault plane, and the stacking fault is related to the deficit of cations. *E* are different nonconservative interfaces because there is 1/4[$\bar{1}\bar{1}1$] displacement of the dots at *E* instead of 1/4[111] displacement at *D*. The structural model is illustrated in Fig. 10, which shows the sequential stacking of two *B* layers similar to that in Fig. 9. It is also a stacking fault, but the ratio of iron and oxygen atoms is 1:1. So the stacking fault is actually related to the excess of cations.

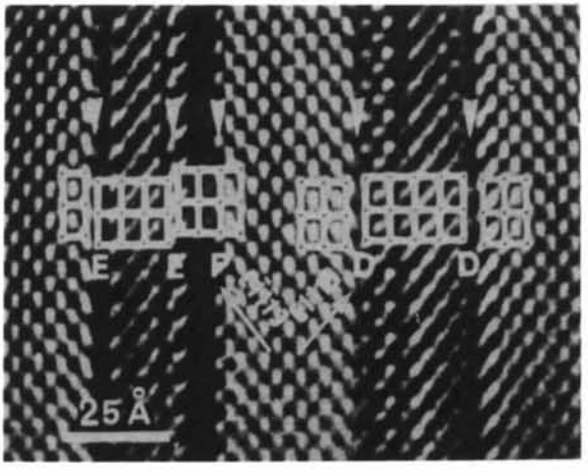

Fig. 8. [1$\bar{1}$0] structural image showing two kinds of nonconservative boundaries labelled *E* and *D* which are 1/4[$\bar{1}\bar{1}$1] and 1/4[111] displacements of dots, respectively, compared with the conservative interface *P*. These defects in the matrix may produce nonstoichiometric structure.

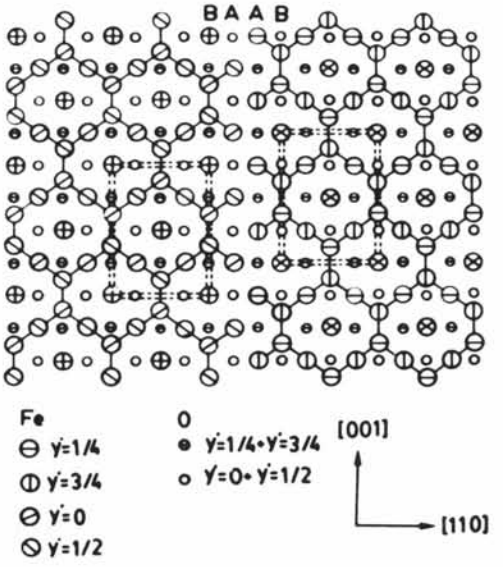

Fig. 9. Stacking fault with an iron to oxygen ratio 2:3 showing a possible arrangement of the iron atoms in the case of cation deficit (see *D* in Fig. 8).

Up to now two kinds of stacking faults related to the ratios of iron and oxygen atoms have been proved. The chemical compositiion will deviate from the regular value of magnetite in local areas in the presence of such defects and the average chemical composition will be unchanged if these two kinds of stacking faults occur in equal numbers. It may be noticed that the framework of oxygen in any of them is perfect and the stacking faults are caused by the arrangement of cations occupying different polyhedral coordinated positions. This suggests that there is some degree of freedom for the occupation of the cations in the framework at the initial stage of nucleation when the fluctuation of cations happened in local areas and this remains in the growing process. In other words, the fluctuation of cations may cause the non-stoichiometry by forming defects in the stoichiometric structure.

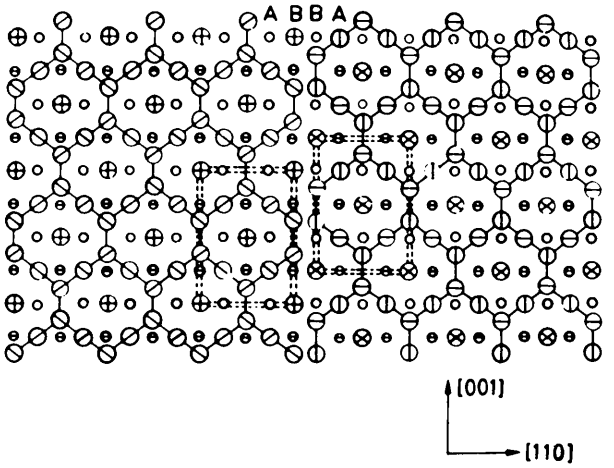

Fig. 10. Stacking fault with an iron to oxygen ratio 1:1 showing a possible arrangement of the iron atoms in the case of cation excess (see *E* in Fig. 8).

All the defects observed are located on the interphase boundaries or in coulsonite, implying that they were pre-existing defects formed in the process of crystallization of an average structure and these positions were favourable for the nucleation of coulsonite when it separates from the average structure in order to reduce the total free energy of the system on cooling. In our observations, cations are always in deficit, although the presence of excess cations is possible in local areas.

References

BAKER, G. S. & WHELAN, M. J. (1968). 4th Eur. Regional Congr. on Electron Microscopy, Rome. Abstracts, pp. 449-450.
CAHN, J. W. (1968). *Trans. Am. Inst. Min. Metall. Pet. Eng.* **242**, 166-180.
DIECKMANN, R. (1982). *Ber. Bunsenges. Phys. Chem.* **86**, 112-116.
DIECKMANN, R. & SCHMALZRIED, H. (1977). *Ber. Bunsenges. Phys. Chem.* **81**, 414-419.
GIBBS, J. M. (1948). *Collected Works*, Vol. 1, pp. 105-115, 252-258. Yale Univ. Press.
HÄGG, G. (1953). *Z. Kristallogr. Teil B*, **29**, 95-99.
ISHIZUKA, K. (1982). *Acta Cryst.* A**38**, 773-779.
RADTKE, A. S. (1962). *Am. Mineral.* **47**, 1284-1291.
RUNBLE, D. (1976). *Oxide Minerals.* Washington: Mineralogical Society of America.

Acta Cryst. (1989). A**45**, 268-274

Description of Hexagonal Frank–Kasper Phases by a Projection Method

BY Z. M. WANG, Q. B. YANG AND K. H. KUO*

Laboratory of Atomic Imaging, Institute of Metal Research, Academia Sinica, 110015 *Shenyang, People's Republic of China*

(*Received* 1 *June* 1988; *accepted* 13 *October* 1988)

Abstract

The structure of hexagonal Frank-Kasper (FK) phases can be described by the projection of the seven-dimensional (7D) Cr_3Si and Zr_4Al_3 cubes in a suitable projection subspace onto a 3D hyperplane. The close relationship between hexagonal FK phases and the dodecagonal quasicrystal with 12-fold rotational symmetry is discussed.

1. Introduction

Significant activity has been generated among condensed-matter physicists and crystallographers by the recent discovery of Bragg diffraction patterns with icosahedral symmetry corresponding to a new quasicrystalline phase of matter. Several 2D and 3D tiling models with noncrystallographic symmetry have been proposed based on the view that a quasilattice is a projection of a higher-dimensional periodic lattice in a defined projection subspace onto a lower-dimensional hyperplane. According to Elser &

* Also at Beijing Laboratory of Electron Microscopy, Academia Sinica, PO Box 2724, 100080 Beijing, People's Republic of China.

0108-7673/89/040268-07$03.00